Microchimica Acta (2021) 188: 69
https://doi.org/10.1007/s00604-021-04726-z

ORIGINAL PAPER

0D/2D heteronanostructure–integrated bimetallic CoCu-ZIF nanosheets and MXene-derived carbon dots for impedimetric cytosensing of melanoma B16-F10 cells

Yang Liu[1] · Shunjiang Huang[2] · Jiangnan Li[1] · Minghua Wang[2] · Changbao Wang[2] · Bin Hu[2] · Nan Zhou[1] · Zhihong Zhang[2]

Received: 29 July 2020 / Accepted: 20 January 2021 / Published online: 5 February 2021

Abstract

A novel heterogeneous architecture has been constructed integrating two-dimensional (2D) bimetallic CoCu–zeolite imidazole framework (CoCu-ZIF) and zero-dimensional (0D) $Ti_3C_2T_x$ MXene-derived carbon dots (CDs) (represented by CoCu-ZIF@CDs). The prepared CoCu-ZIF@CDs were further explored as sensitive layer for anchoring B16-F10 cell–targeted aptamer strands and detecting B16-F10 cells from the biological environment. Basic characterization showed that CDs were homogeneously embedded within CoCu-ZIF NSs owing to their π-π stacking interaction, leading to outstanding fluorescence performance of the 0D/2D CoCu-ZIF@CD nanohybrid. As such, the CoCu-ZIF@CD-based cytosensor was applied to detect living B16-F10 cells through electrochemical techniques and cell imaging. Compared with CoCu-ZIF- and CD-based cytosensors, the constructed CoCu-ZIF@CD-based one showed superior sensing performance, with an extremely low limit of detection (LOD) of 33 cells·mL^{-1} and a wide range of suspension concentration of 1×10^2–1×10^5 cells·mL^{-1} B16-F10 cells. The developed cytosensor also demonstrated excellent detection performance, including cell imaging properties, good selectivity, high stability, and good reproducibility. By anchoring other probe molecules, the constructed CoCu-ZIF@CD-based biosensor can be extensively explored for early diagnosis of other analytes, thereby widening the applications of porous organic frameworks in biosensing and biomedical fields.

Keywords Bimetallic metal-organic frameworks · $Ti_3C_2T_x$ MXene · Carbon dots · Electrochemical cytosensor · Detection of living cancer cells · Early diagnosis of B16-F10 cells

Introduction

Cancer has become one of the most widespread diseases, and early diagnosis of cancer is a key to decreasing death rate and improving survival rate. In this regard, developing credible, sensitive, rapid, and effective approaches for early diagnosis of cancer is of great importance to treatment of cancer patients [1]. Aberrantly expressed tumor markers, namely, special RNA/DNA or living cancer cells, in biological samples are the main analytes for cancer diagnosis, and analysis of living cancer cells is the most direct method for cancer determination [2]. However, traditional techniques, such as X-ray, computed tomography (CT), transrectal ultrasonography, positron emission tomography (PET), magnetic resonance imaging (MRI), B ultrasound, and PET/CT, are focused on morphological changes of tissues and not practical for repeated screenings at early stages of disease. They cannot meet the demand of early and accurate diagnosis of cancer and result in missing the best times for cancer therapy [3–5]. Besides, various methods based on biochemistry, immunology, and molecular biology have been developed to improve the sensitive detection of living cancer cells [6, 7]. Common methods for sensing living cancer cells include surface plasmon resonance, gel electrophoresis, surface-enhanced Raman spectroscopy,

✉ Nan Zhou
fcczhoun@zzu.edu.cn

✉ Zhihong Zhang
mainzhh@163.com

[1] Department of Orthopedics, The First Affiliated Hospital of Zhengzhou University, No. 1, Jianshe East Road, Zhengzhou 450052, People's Republic of China

[2] School of Materials and Chemical Engineering, Zhengzhou University of Light Industry, No. 136, Science Avenue, Zhengzhou 450001, People's Republic of China

colorimetric assay, electrochemical assay, fluorescence methods, and immunohistochemical assays [8]. Among them, owing to simple operation, high selectivity, and fast response, electrochemical sensing is regarded as an ideal tool for cancer diagnosis and is applied to analyze diverse biomarkers and living cancer cells [9–11].

Aptamers are popular for biosensors due to their temperature stability, pH resistance, and simple production [12]. Combining the advantages of aptasensors with those of electrochemical techniques, electrochemical biosensors have aroused increasing attention due to their high sensitivity and superior specificity for detecting various biomarkers or living tumor cells [13, 14]. The signal transducer of electrochemical sensors is usually based on chemical modification of an electrode; thereby, nanomaterial plays a crucial role in enhancing sensitivity and selectivity toward specific target compounds [15]. Diverse nanomaterials, including conducting polymers, carbon-related nanomaterials, electrochemically active substances, quantum dots (QDs), and porous organic frameworks [16], have been employed to construct electrochemical biosensors. A program with reliable, accurate, and intuitive detection, such as combining electrochemical detection with cell imaging, has high feasibility for investigation of living tumor cells.

Metal-organic frameworks (MOFs), which are composed of metal ions linked by organic bridging ligands with ultrahigh porosity and large internal surface area, have been widely used in different fields, such as gas storage, adsorption, contaminant sorption, separation, catalysis, drug delivery, cancer therapy, and chemo/biosensing [17]. MOFs contain organic linkers and thus can strongly adsorb abundant negatively charged aptamer strands via possible π-π stacking, hydrogen bond, and electrostatic interactions. Furthermore, MOF-based derivatives or MOF-based composites have been developed as a promising platform for anchoring probe molecules for constructing different types of biosensors [18]. For instance, a series of bimetallic MOFs or MOF-derivatives have been utilized as bifunctional electrochemical aptasensors for simultaneous detection of biomarkers and overexpressed tumor cells. Bimetallic TbFe-MOFs have been designed by MOF-on-MOF strategy and utilized as a platform for anchoring carbohydrate antigen 125 (CA125) aptamer to detect CA125 and living Michigan cancer foundation-7 (MCF-7) cells; the sensor showed low LOD of 58 $\mu U \cdot mL^{-1}$ and 19 $cells \cdot mL^{-1}$ toward CA125 and MCF-7 cells, respectively [14]. ZrHf-MOF has been applied as a sensitive layer for constructing electrochemical biosensors to detect human epidermal growth factor receptor-2 (HER2) and living HER2-overexpressed MCF-7 cells [13]. Nevertheless, most MOFs have poor electrical conductivity, hindering their applications in the biosensing field. Thus, different approaches have been explored to enhance the electrochemical activity of MOFs; such approaches include combination with other nanomaterials that have high electrochemically activity [11, 19], addition of other electrochemical indicators [20], or calcination of MOFs at high temperatures [20, 21]. However, the fussy preparation procedures or high energy consumption hinders the application of MOF-based sensors in practical diagnosis. Thus, pristine MOFs that could be directly used as platforms for electrochemical biosensors should be prepared.

At present, 2D MOF nanosheets (NSs), which combine the advantages of ultrathin 2D nanomaterials with MOFs, are emerging as promising candidate materials for electrochemical biosensors due to their mechanical flexibility, optical transparency, electrocatalytic performance, and compelling electrochemical properties [22]. Especially, 2D zeolitic imidazolate frameworks (ZIFs) have attracted significant interest. Owing to excellent thermal and chemical stability, large surface area, low cost, and tailorable structures [23], ZIFs show promising applications in biosensing fields. However, most MOFs lack fluorescence performance, leading to difficulty in detecting living cancer cells by using imaging. Entrapping quantum dots into the MOF skeleton networks can provide a potential approach to solve this problem [24]. Most reported quantum dots for MOF modification are noble metal-based nanoclusters or inorganic nanomaterial-based quantum dots, which have high cost or low biocompatibility. $Ti_3C_2T_x$ MXenes have been widely applied in different fields [25, 26] owing to their excellent properties such as good electrical conductivity, hydrophilicity, large surface, and easy film formation. Reducing the lateral sizes of MXene to several nanometers produces photoluminescent MXene carbon dots (CDs) that have large surface area, better solvent-free solubility, and easy hybridization/blending with other nanomaterials to obtain tunable fluorescence and biocompatibility. CDs have been considered an emerging active material in biosensing [27], cell imaging, and cancer therapy [28].

Considering the individual features of 2D MOFs NSs and CDs and the synergistic effect of 0D/2D heterojunction nanostructures, scholars should develop composites of 2D MOF NSs and 0D CDs. In this study, we aim to construct a novel bifunctional platform for the detection of living cancer cells and cell imaging. B16-F10 melanoma cells were used as model cells. DNA aptamer sgc-8 exhibited specific binding and high affinity toward PTK7 receptor that was overexpressed in B16-F10 melanoma cells [29]. For the first time, we designed and synthesized a novel 0D/2D heterogeneous architecture of MXene-derived CDs embedded with bimetallic CoCu-ZIF NSs (represented by CoCu-ZIF@CDs). The obtained CoCu-ZIF@CDs heteroarchitecture demonstrated superior electrochemical properties, mixed metal valence states of coordinated centers, good fluorescent performance, and remarkable biocompatibility owing to efficient integration of 2D CoCu-ZIF NSs and 0D CDs. The porous nanostructure composed of nanosheets and embedded with large amounts of CDs

endowed the constructed cytosensor with outstanding electrochemical activity and strong fluorescence performance; the porous nanostructure also provided exposed active sites, which can impel the aptamer strands to strongly anchor owing to π-π stacking interaction, electrostactic force between nitrogen-related groups and aptamer strands, and Van der Waal force [30]. The synergism among these factors results in superior sensing performance for detection of living cancer cells through electrochemical techniques and cell imaging. As such, the fabricated CoCu-ZIF@CD-based cytosensor displayed an extremely low LOD of 33 cells·mL^{-1} within the wide range of the suspension concentration of 1×10^2–1×10^5 cells·mL^{-1} B16-F10 cells and good selectivity toward normal mouse cells L929. The present work not only presents a potential application of MOF-related complexes in sensing fields but also provides a promising way for early diagnosis of cancer biomarkers.

Experimental section

The parts of chemicals and reagents, synthesis of the CoCu-ZIF NSs and CDs, pretreatment of the bare Au electrode (AE), preparation of all solutions, preparation of the suspensions of living cells, and basic characterizations are provided in the S1 (see Supplementary information).

Sensor design

As illustrated in Scheme 1, the construction of cytosensors based on CoCu-ZIF@CD nanohybrid includes four steps: preparation of CoCu-ZIF@CD nanohybrid, modification of AE with CoCu-ZIF@CD nanohybrid, aptamer immobilization, and detection of B16-F10 cells. Once the CoCu-ZIF@CD nanohybrid is prepared, its homogeneous suspension is deposited onto the AE surface. Owing to the nanoscale size of the CoCu-ZIF@CD nanohybrid and the specific skeleton of the MOF framework [20], the contact and close adhesion force between the nanohybrid and AE occur, resulting in the stabilized nanohybrid layer over the electrode. The aptamer, which is targeted with B16-F10 cancer cells with the sequence of 5′-ATC TAA CTG CTG CGC CGC CGG GAA AAT ACT GAT CGG TTA GA-3′, is anchored onto the CoCu-ZIF@CDs nanohybrid due to π-π stacking interaction, electrostatic interaction between positively charged nitrogen-related groups and negatively charged phosphate groups of aptamer strands, and Van der Waals force [31]. The immobilization of a large amount of aptamer strands can efficiently reduce non-specific adsorption between living cells and the nanohybrid due to the porous network, large specific surface area, and exposed anchoring sites. In the presence of B16-F10 cancer cells, the aptamer strands must change its conformation to binding to the living cancer cells owing to the specific recognition between them [32]. Furthermore, the porous and intrinsic skeleton network of CoCu-ZIF produces sufficient space for aptamer strands to adjust its conformation. Modification of AE, immobilization of aptamer strands, and detection of living cells alter the electrochemical performance of the electrode. The excellent electrochemical activity of the CoCu-ZIF@CD nanohybrid can effectively transduce slight changes and ensure outstanding sensing performance.

Preparation of the CoCu-ZIF@CD nanohybrid

The preparation of CoCu-ZIF NSs was referred to the reported literature with a slight modification [33, 34]. Furthermore, the CDs were prepared according to the reference [35]; details are supplied in the S1.2 section (see Supplementary information).

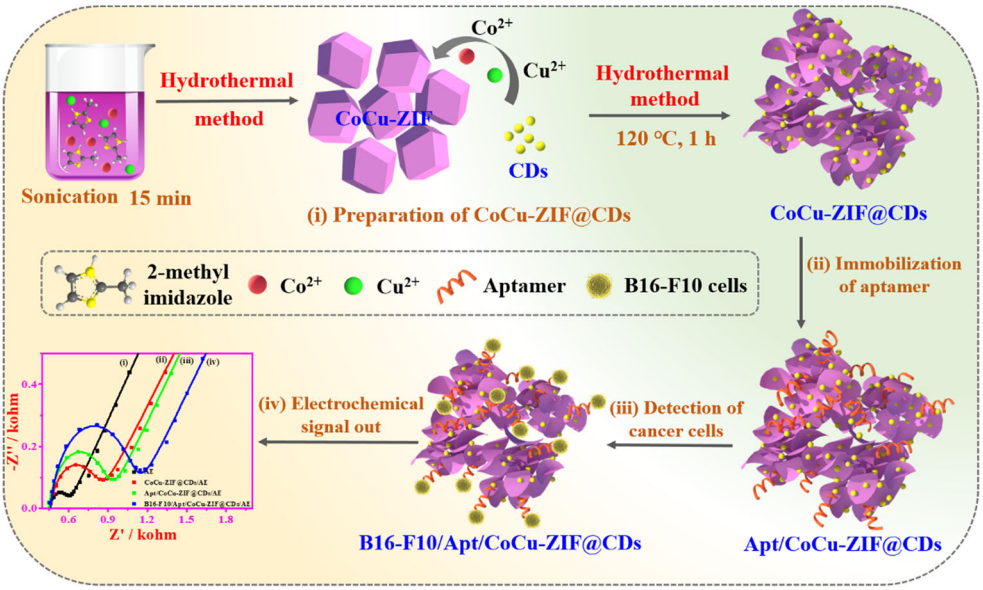

Scheme 1 Schematic diagram of the CoCu-ZIF@CD-based cytosensor for the detection of B16-F10 cells, including (i) the preparation of CoCu-ZIF@CDs hybrid, (ii) the immobilization of aptamer on CoCu-ZIF@CDs/AE, and (iii) the detection of B16-F10 cells

For the synthesis of CoCu-ZIF@CDs, 0.55 g of Co $(NO_3)_2 \cdot 6H_2O$ and 0.55 g of $Cu(NO_3)_2 \cdot 6H_2O$ were dissolved in 30 mL of methanol to form solution I. A total of 1.32 g of 2-methyl imidazole was dissolved in 30 mL of methanol to form solution II. Then, solution I was quickly added into solution II followed by sonication for 15 min. The mixture was washed with methanol and separated by centrifugation to obtain CoCu-ZIF powder. Subsequently, the CoCu-ZIF powder and the suspension of CDs (2 mg·mL^{-1}, 10 mL) were dispersed in methanol (30 mL) and mixed with another copy of solution I. Afterward, the mixture was moved into a Teflon-lined stainless-steel autoclave (100 mL) and heated at 120 °C for 1 h. Finally, the resultant product was rinsed by methanol several times and separated by centrifugation, followed by drying at 60 °C overnight. As such, CoCu-ZIF@CDs were obtained.

Fabrication of the electrochemical cytosensors

Here, the cytosensor based on CoCu-ZIF@CDs nanohybrid was developed to detect the living B16-F10 cells. Firstly, the CoCu-ZIF@CDs nanohybrid with different dosages (1, 2, 5, 10, and 20 mg) was separately dispersed in 10 mL Milli-Q water and stayed by ultrasound for 30 min to form a homogeneous aqueous suspension with different concentrations of 0.1, 0.2, 0.5, 1.0, and 2.0 mg·mL^{-1}. Then, 5.0 μL of the CoCu-ZIF@CDs suspension was dropped onto the pretreated AE surface (represented by CoCu-ZIF@CDs/AE), followed by drying under nitrogen. Subsequently, the CoCu-ZIF@CDs/AE was immersed in 0.1 M phosphate buffer (pH 7.4) to remove the weakly bonded nanomaterial. Afterward, the CoCu-ZIF@CDs/AE was incubated in the sgc-8 aptamer solution (denoted as Apt/CoCu-ZIF@CDs/AE) for 2 h, followed by rinsing with phosphate buffer sufficiently to remove the excess aptamer strands and drying under nitrogen. Then, the developed Apt/CoCu-ZIF@CDs/AE cytosensor was obtained and stored at 4 °C in a refrigerator prior to the detection of B16-F10 cells (denoted by B126-F10/Apt/CoCu-ZIF@CDs/AE). For comparison, the suspensions of CoCu-ZIF NSs and CDs were also prepared and used to construct cytosensors. The CoCu-ZIF- and CDs-based cytosensors were developed by a similar procedure. Accordingly, each step for the construction of the CoCu-ZIF-based cytosensor was represented by CoCu-ZIF/AE, Apt/CoCu-ZIF/AE, and B126-F10/Apt/CoCu-ZIF/AE, while these steps of the CD-based cytosensor were denoted as CDs/AE, Apt/CDs/AE, and B126-F10/Apt/CDs/AE, respectively.

Electrochemical measurements

The full description about the electrochemical measurements was provided in the S1.7 section and Fig. S1. The modified AE, Ag/AgCl (saturated KCl) electrode, and platinum wire were used as the working electrode, reference electrode, and counter electrode, respectively. Diverse electrochemical techniques such as electrochemical impedance spectroscopy (EIS) and cyclic voltammetry (CV) were performed to probe the cytosensor fabrication and detection of living cells in the mixture of 5.0 mM $K_3[Fe(CN)_6]/K_4[Fe(CN)_6]$ (1:1) as a redox probe dissolved in 0.1 M phosphate buffer. CV curves were measured at potential ranging from − 0.2 to 0.8 V vs. Ag/AgCl at the scan rate of 100 mV s^{-1}, while the EIS Nyquist plots were recorded within the frequency range of 0.01 Hz–100 kHz with amplitude of 5 mV under open circuit potential.

To obtain the superior sensing performance for the detection of B16-F10 cells, different measurement parameters were optimized, including the dosages of the CoCu-ZIF@CD suspension (0.1, 0.2, 0.5, 1.0, and 2.0 mg mL^{-1}), the concentration of aptamer solution (10, 20, 50, 100, 200, and 500 nM), and the binding time of the B16-F10 cells.

The LOD of the developed CoCu-ZIF@CD-based cytosensor for detecting B16-F10 cells was investigated under optimal measurement conditions. In this regard, the Apt/CoCu-ZIF@CDs/AE was separately incubated with the B16-F10 cells suspensions with different concentrations (1×10^2, 5×10^2, 1×10^3, 5×10^3, 1×10^4, and 1×10^5 cells·mL^{-1}). The calibration plot was obtained by plotting EIS responses (charge-transfer resistance, R_{ct}) and logarithm of the B16-F10 cell concentrations. The LOD of the developed cytosensor was calculated according to the criterion of IUPAC recommendation. To determine the selectivity of the developed cytosensor, the normal mice cells (L929 cells) were applied as the interferent. The EIS response (R_{ct}) caused by detecting L929 cells was compared with that of B16-F10 cells. Furthermore, other kinds of cancer cells, such as MCF-7, 4T1, K7M2, and CT26 (1×10^3), were also utilized as the targeted cells for evaluating the selectivity of the developed cytosensor. Different cancer markers and protein, including prostate specific antigen (PSA), epidermal growth factor receptor (EGFR), alpha fetoprotein (AFP), vascular endothelial growth factor (VEGF), myoglobin (Mb), troponin (Tn), and immunoglobulin G (IgG) (10 pg·mL^{-1}), which could be coexisted with PTK7, were also used for investigating the selectivity of the proposed cytosensor, as well as the detection of PTK7 (0.1 pg·mL^{-1}).

The reproducibility of the CoCu-ZIF@CD-based cytosensor was determined by measuring five independent Apt/CoCu-ZIF@CDs/AEs toward B16-F10 cells with three concentrations of 5×10^2, 1×10^3, and 5×10^3 cells mL^{-1} and compared their electrochemical responses. The stability of the constructed cytosensor was assessed by storing Apt/CoCu-ZIF@CDs/AE in a refrigerator (4 °C) for 15 days and continuously detecting B16-F10 each day by EIS technique.

Results and discussion

Basic characterizations of the CoCu-ZIF@CDs nanohybrid

Surface morphology and nanostructure were identified by SEM and TEM images. As illustrated in Fig. S2a-b, the as-prepared CoCu-ZIFs are composed of loose nanospheres, which are assembled with large amounts of NSs. TEM image (Fig. S2c) of the CoCu-ZIF shows the hollow vesicle structure comprising ultrathin NSs. The unique structure improves the specific surface area of CoCu-ZIF NSs, thereby promoting electron transfer and enhancing the electrochemical activity of CoCu-ZIF NSs [36]. The high-resolution HR-TEM (HR-TEM) image of CoCu-ZIF NSs (Fig. S2e) shows no clear lattice fringe, suggesting its low crystallinity. The TEM and HR-TEM images of CDs are illustrated in Fig. S3. CDs show clear nanodots with size of 2–5 nm. The lattice fringes with interlayer distances of 0.23 and 0.26 nm are observed in the HR-TEM image (Fig. S3c), corresponding to the (103) and (110) planes of $Ti_3C_2T_x$ [37]. The interlayer distance of 0.29 nm is assigned with graphite [38]. This finding suggests that CDs derived from $Ti_3C_2T_x$ exhibit the features of MXene and carbon quantum dots. As demonstrated in Fig. 1a and b, the SEM images of the synthesized CoCu-ZIF@CDs nanohybrid show a globular and worm-like structure. Owing to the existence of CDs, the regularly hollow vesicle of CoCu-ZIF NSs is replaced by the disordered accumulated nanosheets. This finding is further confirmed by the TEM images (Fig. 1c and d), where large amounts of nanodots are embedded within the nanosheets. The clear lattice fringes of 0.23, 0.26, and 0.29 nm are observed in the HR-TEM image of CoCu-ZIF@CDs nanohybrid, which originate from CDs. This result confirms the successful combination of CoCu-ZIF NSs and CDs. As shown in Fig. 1f, the corresponding elemental mapping analysis demonstrates the uniform distribution of Co, Cu, C, and N throughout the CoCu-ZIF@CD nanohybrid.

The crystalline and chemical structures of CoCu-ZIF NSs, CDs, and CoCu-ZIF@CDs nanohybrid were characterized by X-ray diffraction (XRD) spectroscopy, Fourier transform infrared spectroscopy (FT-IR), Raman spectroscopy, and X-ray photoelectron spectroscopy (XPS) analyses. As shown in Fig. S4a, four distinctive diffraction peaks located at 9.9°, 19.7°, 33.8°, and 60.1° in CoCu-ZIF NSs (curve *i*) are assigned with the diffraction peaks of ZIF and consistent with literature [36]. After doping with large amounts of CDs, the peaks ascribed to CoCu-ZIF NSs disappear. The 2θ peaks at 16.2°, 32.09°, and 39.3° are observed in CoCu-ZIF@CDs nanohybrid (curve *ii*) corresponding to (104) of Ti_3AlC_2 [39]. Moreover, the FT-IR spectrum of CoCu-ZIF NSs (curve *i*) (Fig. S4b**)** shows the peak at 3454 cm^{-1}, which is attributed to –OH stretching vibration, and the peak at 2925 cm^{-1}, which is related to C–H vibration from the alkyl chain. The peaks at 1630 and 1365 cm^{-1} are attributed to C=O and in-plane rocking of O-H, respectively. Meanwhile, the peak at 1045 cm^{-1} is assigned to the C–O stretching vibration [40]. The FT-IR spectrum of the CoCu-ZIF@CDs nanohybrid (curve *ii*) (Fig. S4b) indicates new peaks at 1136 and 870 cm^{-1}, which are ascribed to C–O/C–N and aromatic (C–H), respectively. The peak located at 636 cm^{-1} is due to Ti-O bending [27].

The Raman spectra of CoCu-ZIF NSs and CoCu-ZIF@CDs nanohybrid are displayed in Fig. S4c. The CoCu-ZIF NSs (curve *i*) show bands centered at ~ 462 and 518 cm^{-1}, which are related to the vibrational modes of E_g and ${F_{2g}}^2$ of metal-O vibrations in CoCu-ZIF NSs; the weak band at 1056 cm^{-1} is ascribed to the deformation mode of hydroxyl [25, 41]. The CoCu-ZIF@CDs nanohybrid exhibits the similar bands with CoCu-ZIF NSs. Moreover, the photo-induced luminescent spectrum of CDs is obtained using a fluorescence spectrophotometer at room temperature (Fig. S4d). A narrow and strong emission band centered at 640 nm and a small peak at 743 nm with an excitation wavelength of 428 nm. The PL emission spectrum of CoCu-ZIF@CD nanohybrid shows similar characteristics of CDs (Fig. S4e). These results manifest that the fluorescent CoCu-ZIF@CD nanohybrid can be employed for cell imaging.

The chemical structure and components of CoCu-ZIF@CDs nanohybrid are determined by XPS characterization. As displayed in Fig. 1g, the Cu $2p_{3/2}$ peak can be split into four parts, in which the binding energy (BE) levels at 934.6 and 935.7 eV are attributed to Cu^+ and Cu^{2+}, along with their satellite peaks at BE of 940.6 and 943.5 eV, respectively. The Co $2p_{3/2}$ XPS peak (Fig. 1h) is deconvoluted into four components at BE levels of 781, 783, 786.4, and 789.3 eV, which are assigned to Co^{3+}, Co^{2+}, and their corresponding satellite peaks, respectively. The mixed metal valence states of Cu^+/Cu^{2+} and Co^{2+}/Co^{3+} exist in the CoCu-ZIF@CDs nanohybrid. These mixed metal valences of Co and Cu can greatly enhance the electron transfer in aqueous solution and amplify the sensing signal [42]. The C 1*s* XPS spectrum in Fig. 1i indicates four main components including C–C, C–O, C=O, and COO groups, which originate from the ligand linker of CoCu-ZIF NSs and CDs. XPS characterization of CoCu-ZIF NSs is also probed (Fig. S5). Similar deconvoluted peaks of Cu 2*p* and Co 2*p* are observed for CoCu-ZIF NSs, but no C=O peak appears in the C 1*s* XPS spectrum. Furthermore, the high-resolution C 1*s* XPS spectrum of CDs is fitted, showing the peaks at the BE levels of 284, 284.6, 286, 288.3, and 291 eV, which are attributed to C=C, C–C, C–O, COO, and π-π^* species (Fig. S6). Compared with CoCu-ZIF and CoCu-ZIF@CDs, the C=C group is dominant in the C 1*s* XPS peak of CDs, which is due to the conjugated nanostructure of CDs and π-π^* binding. Moreover, no clear Ti 2*p* signal of CDs is observed, suggesting the formation of pure carbon dots. The XPS results reveal that the CoCu-ZIF@CD nanohybrid

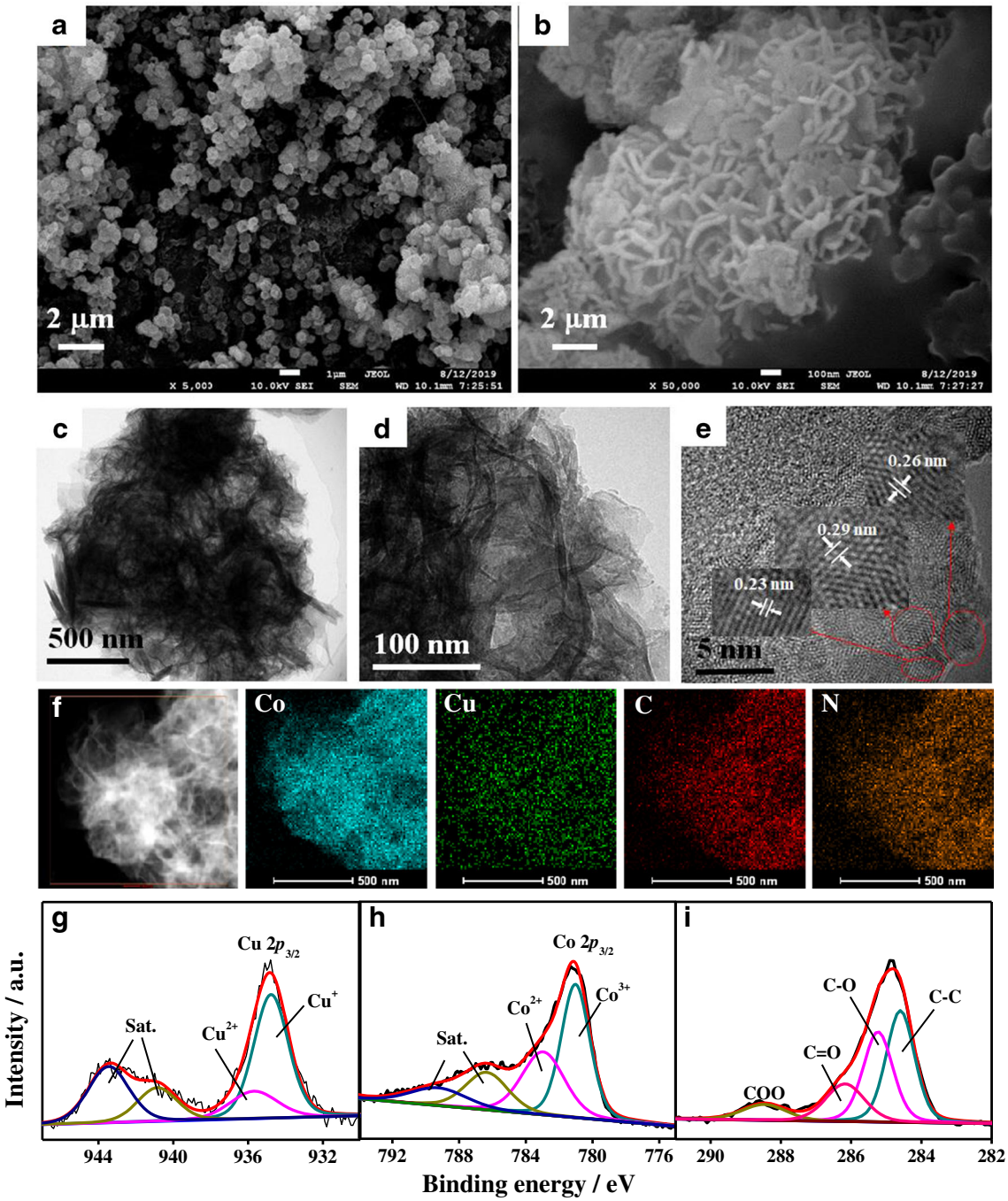

Fig. 1 (**a**, **b**) Low- and high-magnification SEM and (**c**, **d**, **e**) TEM and HR-TEM images of CoCu-ZIF@CDs nanohybrid. (**f**) Elemental mapping of homogenously distributed Co (blue), Cu (green), C (red), and N (brown) containing in CoCu-ZIF@CDs nanohybrid. High-resolution XPS spectra of (**g**) Cu 2*p*, (**h**) Co 2*p*, and (**i**) C 1*s* of CoCu-ZIF@CDs nanohybrid

contains mixed metal valence states and multiple functional groups, which can facilitate the electrochemical activity and binding affinity toward aptamers.

Cell imaging of the CoCu-ZIF@CDs nanohybrid

The biocompatibility or cytotoxicity of the CoCu-ZIF@CDs nanohybrid was investigated (see S3 and Fig. S7 in the Supplementary Material). The cellular uptake behavior of the CoCu-ZIF@CDs nanohybrid against normal L929 cell line and cancerous B16-F10 cell line was examined by confocal laser scanning microscopy (CLSM). As shown in Fig. 2, weak green fluorescence signals were observed both in L929 cells and B16-F10 cells. Compared with the blue fluorescence of Hoechst 33342 stained in the nuclei, the green fluorescence of the CoCu-ZIF@CDs nanohybrid is mainly located in the

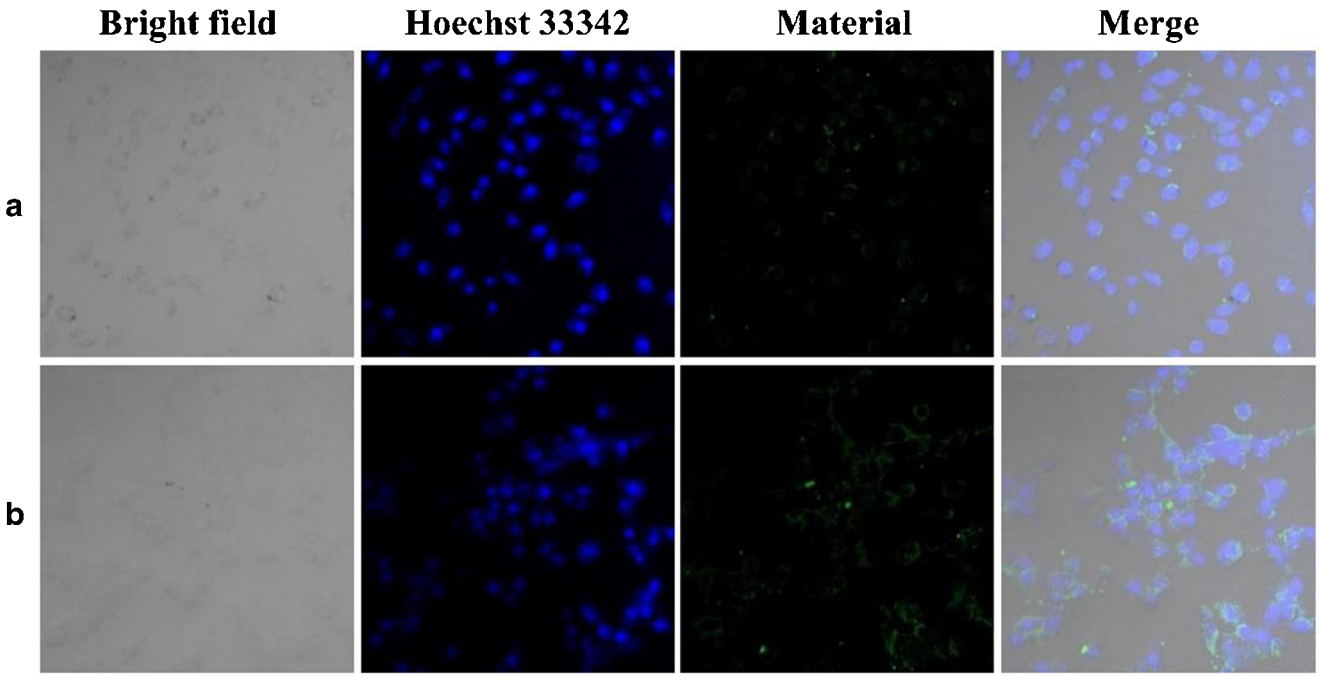

Fig. 2 Cellular uptake behaviors of CoCu-ZIF@CDs nanohybrid incubated with (**a**) L929 cells and (**b**) B16-F10 cells for 1 h. Nucleus-staining Hoechst 33342 showed blue fluorescence, and CoCu-ZIF@CDs showed green fluorescence. Colocalization staining in merged picture showed the intracellular distribution of CoCu-ZIF@CDs in L929 and B16-F10 cells

cytoplasm. The results indicate that a small amount of the CoCu-ZIF@CDs nanohybrid can be absorbed on the surface of B16-F10 cells and L929 cells through non-specific interaction. After immobilizing with the DNA aptamer sgc-8, the cellular uptake behavior of Cy3-Apt/CoCu-ZIF@CDs incubated with the suspensions of L929 and B16-F10 cells was further investigated by CLSM (Fig. 3). Cy3-Apt/CoCu-ZIF@CDs display strong yellow and green fluorescence intensity against B16-F10 cells, while weak yellow and green fluorescence signals were observed in L929 cells. The results indicate that Cy3-Apt/CoCu-ZIF@CDs can be accumulated within the cytoplasm by endocytosis after the specific recognition between the aptamer and receptor of cancer cells. The specific cell uptake results of Cy3-Apt/CoCu-ZIF@CDs

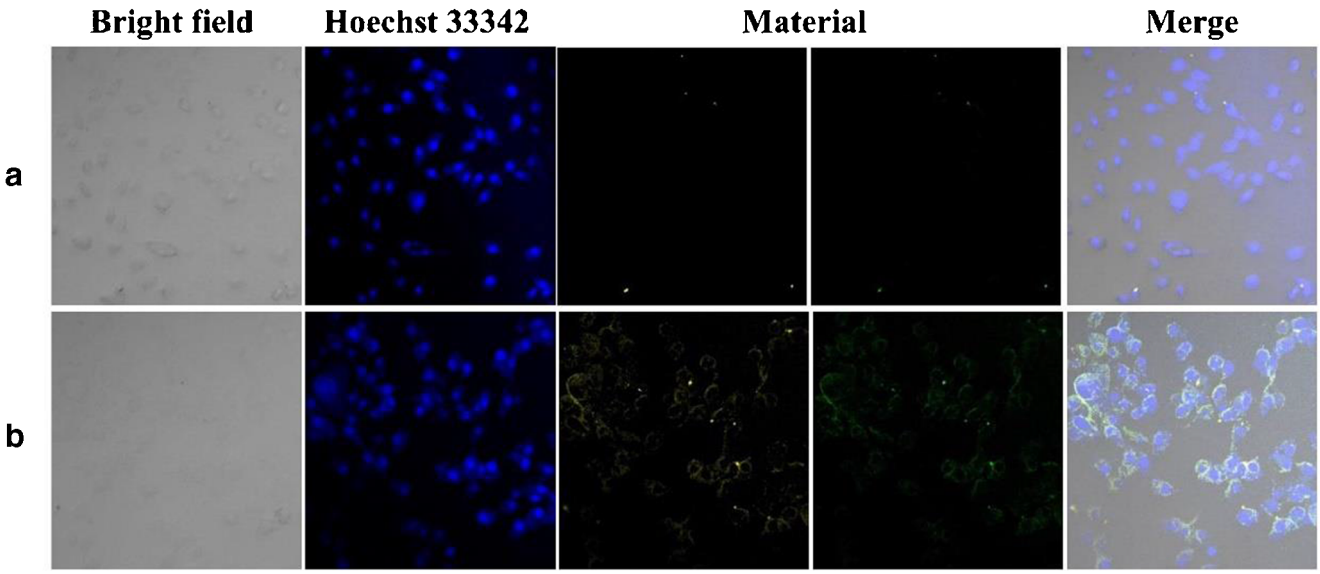

Fig. 3 Cellular uptake behaviors of Apt/CoCu-ZIF@CDs nanohybrid incubated with (**a**) L929 cells and (**b**) B16-F10 cells for 1 h. Nucleus-staining Hoechst 33342 showed blue fluorescence, and Cy3-Apt/CoCu-ZIF@CDs showed yellow fluorescence from Cy3 and green fluorescence from CDs. Colocalization staining in merged picture showed the intracellular distribution of Cy3-Apt/CoCu-ZIF@CDs in L929 and B16-F10 cells

against L929 cells and B16-F10 cells reveal that it can be applied as a cytosensor to sensing living cancer cells.

Electrochemical performance of CoCu-ZIF@CD-based cytosensor for detecting living B16-F10 cells

Three kinds of cytosensors were fabricated based on CoCu-ZIF NSs, CDs, and CoCu-ZIF@CDs nanohybrid for sensing living B16-F10 cells. Each step of the cytosensor fabrication and detection of B16-F10 cells was investigated by EIS and CV (Figs. 4a and S8). The results of the three cytosensors for detecting B16-F10 cells are similar to the electrochemical results. The R_{ct} values for each step during the cytosensor fabrication and detection of cells for all cytosensors were deduced from EIS plots and simulated from the equivalent circuit (Table S1). For CoCu-ZIF@CDs-based cytosensors, the EIS Nyquist plots (Fig. 4a) indicate that the pretreated bare AE demonstrates a small R_{ct} value (144.2 Ω), indicating the good electrochemical activity of AE and fast electron transfer between the AE surface and liquid interface. After treating the bare AE with the CoCu-ZIF@CDs nanohybrid, the R_{ct} value of CoCu-ZIF@CDs/AE increases to 365.3 Ω, which may be attributed to the interface formed by the physical adsorption of the CoCu-ZIF@CDs nanohybrid on the bare AE hindering the electron transfer. A higher R_{ct} value of Apt/CoCu-ZIF@CDs/AE (445.3 Ω) is obtained because of the repulsion interaction between the negatively charged phosphate groups and the redox couple of $[Fe(CN)_6]^{3-/4-}$, leading to the slow electron transfer at the solid and liquid interface [43]. When incubated with the suspension of B16-F10 cells, the R_{ct} value of B16-F10/Apt/CoCu-ZIF@CDs/AE increases to 630.3 Ω, which is attributed to the complex formation between B16-F10 cells and aptamer. For the CoCu-ZIF-based cytosensor, the R_{ct} value of CoCu-ZIF/AE is 275 Ω, which is smaller than that of CoCu-ZIF@CDs/AE, indicating its outstanding electrochemical activity. After the aptamer immobilization and detection of B16-F10 cells, Apt/CoCu-ZIF/AE and B16-F10/Apt/CoCu-ZIF/AE exhibit large R_{ct} values of 319 and 392 Ω, respectively. In general, the change in R_{ct} values of each step can be utilized to represent the amount of analyte on the electrode surface [44]. Hence, the variation in R_{ct} values ($\Delta R_{ct} = R_{ct,\,i+1} - R_{ct,\,i}$) of each step was calculated (Fig. 4b) to compare the detection sensitivity of different sensitive layers. Among these samples, CoCu-ZIF/AE shows the smallest ΔR_{ct} (130.2 Ω) owing to its superior electrochemical activity. The presence of CoCu-ZIF NSs can greatly enhance the electrochemical performance, thereby improving the electrochemical biosensing ability. After binding the aptamer strands, the ΔR_{ct} value of Apt/CoCu-ZIF@CDs/AE is 80 Ω, which is higher than that of Apt/CoCu-ZIF/AE (44 Ω), suggesting its higher aptamer binding ability. The amount of aptamer immobilization can affect the sensitivity of biosensor. The ΔR_{ct} values caused by the detection of B16-F10 cells by using CoCu-ZIF- and CoCu-ZIF@CD-based cytosensors are 73 and 185 Ω, respectively. The CoCu-ZIF@CD-based cytosensor exhibits the outstanding sensing performance for the detection of B16-F10 cells due to the excellent electrochemical activity of CoCu-ZIF NSs and excellent biocompatibility. Thus, CoCu-ZIF@CDs is used as a biological platform for the present cytosensor.

The following experimental parameters for the detection of B16-F10 cells were optimized by EIS measurements: (a) the dosage of the CoCu-ZIF@CDs on the cytosensor fabrication; (b) concentration of the aptamer solution; (c) binding time with B16-F10 cells. In short, the following experimental conditions were found to give best results: (a) dosage of CoCu-ZIF@CDs of 1 $mg{\cdot}mL^{-1}$; (b) aptamer concentration of 100 nM; (c) and binding time with B16-F10 cells for 1 h (see S5 and Fig. S9 in the Supplementary information).

Sensitivity of the proposed cytosensor

Under the optimal conditions, the sensing performance of the CoCu-ZIF@CDs-based cytosensor was tested. As demonstrated in Fig. 5a, the constructed cytosensor was separately incubated with the suspensions of B16-F10 cells with

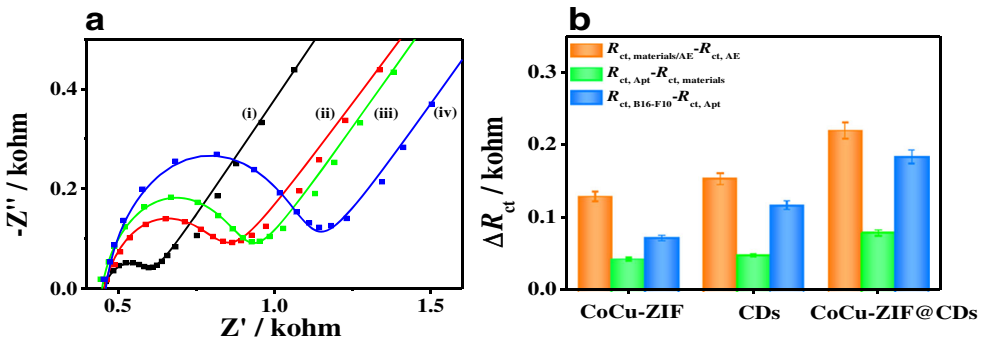

Fig. 4 **a** EIS Nyquist plots of the B16-F10 cells detection procedures using the electrochemical cytosensor based on CoCu-ZIF@CDs nanohybrid in 0.1 M phosphate buffer (pH 7.4) containing 5 mM $[Fe(CN)_6]^{3-/4-}$, including (i) AE, (ii) CoCu-ZIF@CDs/AE, (iii) Apt/CoCu-ZIF@CDs/AE, and (iv) B16-F10/Apt/CoCu-ZIF@CDs/AE. **b** Variations in R_{ct} for each stage in the fabrication procedure of different cytosensors for detection of B16-F10, for which the ΔR_{ct} represents the difference of R_{ct} caused by each step ($\Delta R_{ct} = R_{ct,i+1} - R_{ct,i}$)

different concentrations ranging from 1×10^2 to 1×10^5 cells·mL^{-1} and investigated by EIS technique. The caused EIS responses increase with increasing the B16-F10 cell concentrations, verifying the increased combination between aptamer strands and cancer cells. When B16-F10 cell concentration is larger than 1×10^4 cells·mL^{-1}, the rising trend for detecting B16-F10 is slowly up to a level-off, suggesting the saturated combination between aptamer and cancer cells. The obtained ΔR_{ct} values for detecting B16-F10 cells are also calculated (Fig. 5b). Taking the caused ΔR_{ct} values as the function of the logarithm of the suspension concentration for B16-F10 cells (inset of Fig. 5b), a good linear relationship is observed within the suspension concentration of B16-F10 cells ranging from 1×10^2 to 1×10^5 cells·mL^{-1}. According to the IUPAC method, the LOD is deduced to be 33 cells·mL^{-1} within the B16-F10 concentration range from 1×10^2 cells·mL^{-1} to 1×10^5 cell·mL^{-1} on the basis of:

$$\mathrm{LOD} = 3S_b/m$$

in which S_b represents the standard deviation, and m represents the slope in reference to the gradient of calibration graph. Compared with other nanomaterial-based electrochemical or electrochemiluminescent biosensors (Table 1), the as-fabricated CoCu-ZIF@CD-based cytosensor presents superior sensing performance toward living cancer cells with a broad linear range and low LOD. The extremely low LOD of the present sensing system for detecting living cancer cells is mainly attributed to the specific features of the used electrode nanomaterial of CoCu-ZIF@CDs nanohybrid. The four apparent advantages are as follows: (i) the integration of different metal valence states of Co^{2+}/Co^{3+} and Cu^{2+}/Cu^{+} boosts the electrochemical activity and facilitate the aptamer immobilization, further stabilizing the combination of cancer cells and aptamer strands; (ii) the ultrathin CoCu-ZIF NSs structure not only endows the nanohybrid with excellent electrochemical activity but also provide a robust scaffold for loading large amounts of CDs; (iii) the CDs derived from $Ti_3C_2T_x$ nanosheets exhibit good biocompatibility and strong binding affinity toward aptamer strands; and (iv) the synergistic effect among these factors can tremendously enlarge the electrochemical signal and enhance the sensing performance. Moreover, the fluorescence of CoCu-ZIF@CDs nanohybrid can make the possibility for detecting cancer cells by the fluorescence spectroscopy besides electrochemical techniques.

The selectivity of the cytosensor is an essential factor for practical application. Here, the developed CoCu-ZIF@CDs-based cytosensor was used to detect normal L929 cells to test its selectivity. As shown in Fig. 5c and d, the EIS Nyquist plots for the detection procedure of L929 cells were recorded, in which no clear variation in EIS responses is observed before and after detection. No specific combinations were observed between the aptamer strands and L929 cells, suggesting good selectivity of the present sensor. When the present sensing strategy was used to detect other kinds of cancer cells, such as MCF-7, 4T1, K7M2, and CT26, substantial EIS and CV responses are observed (Fig. S10), as well as large ΔR_{ct} values (Table S2). The explored aptamer strands can combine with some cancer biomarkers that are overexpressed in these cancer cells. Since PTK7 are overexpressed with B16-F10 cells, PTK7 was adopted as a cancer biomarker to investigate the sensing performances of CoCu-ZIF@CDs as biosensor. As expected, Fig. S11 indicates that the remarkable change in the EIS signals for detecting PTK7, along with a large ΔR_{ct} value (326 Ω). Also, the good selectivity of the present CoCu-ZIF@CDs-based cytosensor was obtained when detecting PTK7. As seen from Fig. S12, other interferents, including PSA, EGFR, AFP, $VEGF_{165}$, Mb, Tn, and IgG, did not cause the substantial R_{ct} change. This finding indicates that the as-proposed cytosensor not only can detect some cancer cells but also can determine cancer biomarkers. The shortcoming of

Table 1 An overview on the recently reported nanomaterial-based electrochemical methods for determination of living cancer cells

Materials used	Method applied	Analyte (cells)	Detection range (cells·mL^{-1})	LOD (cells·mL^{-1})	Refs.
$Cu_xNi_{3-x}(HHTP)_2$ MOF	EIS	C6	$50–1 \times 10^5$	21	[45]
Polypyrrole-GCE	EIS	MCF-7	$1 \times 10^2–1 \times 10^5$	100	[46]
Polyacrylonitrile/polypyrrole nanofibers	EIS	A549	$5 \times 10^3–1 \times 10^5$	1.2×10^3	[47]
CdS-coated-ZnO nanorod	Electrochemiluminescence (ECL)	HepG2	$300–1 \times 10^4$	256	[48]
TU-MoS_2	EIS	HepG2	$50–1 \times 10^6$	50	[49]
GQD-ConA@Fe_3O_4	Differential pulse voltammetry (DPV)	Hela	$5 \times 10^2–1 \times 10^5$	273	[50]
DNA bridge-AgNCs	DPV	HepG2	$50–2 \times 10^6$	15	[51]
Au NCs	EIS	MCF-7	$1 \times 10^2–1 \times 10^6$	80	[52]
CoCu-ZIF@CDs	EIS	B16-F10	$1 \times 10^2–1 \times 10^5$	33	This work

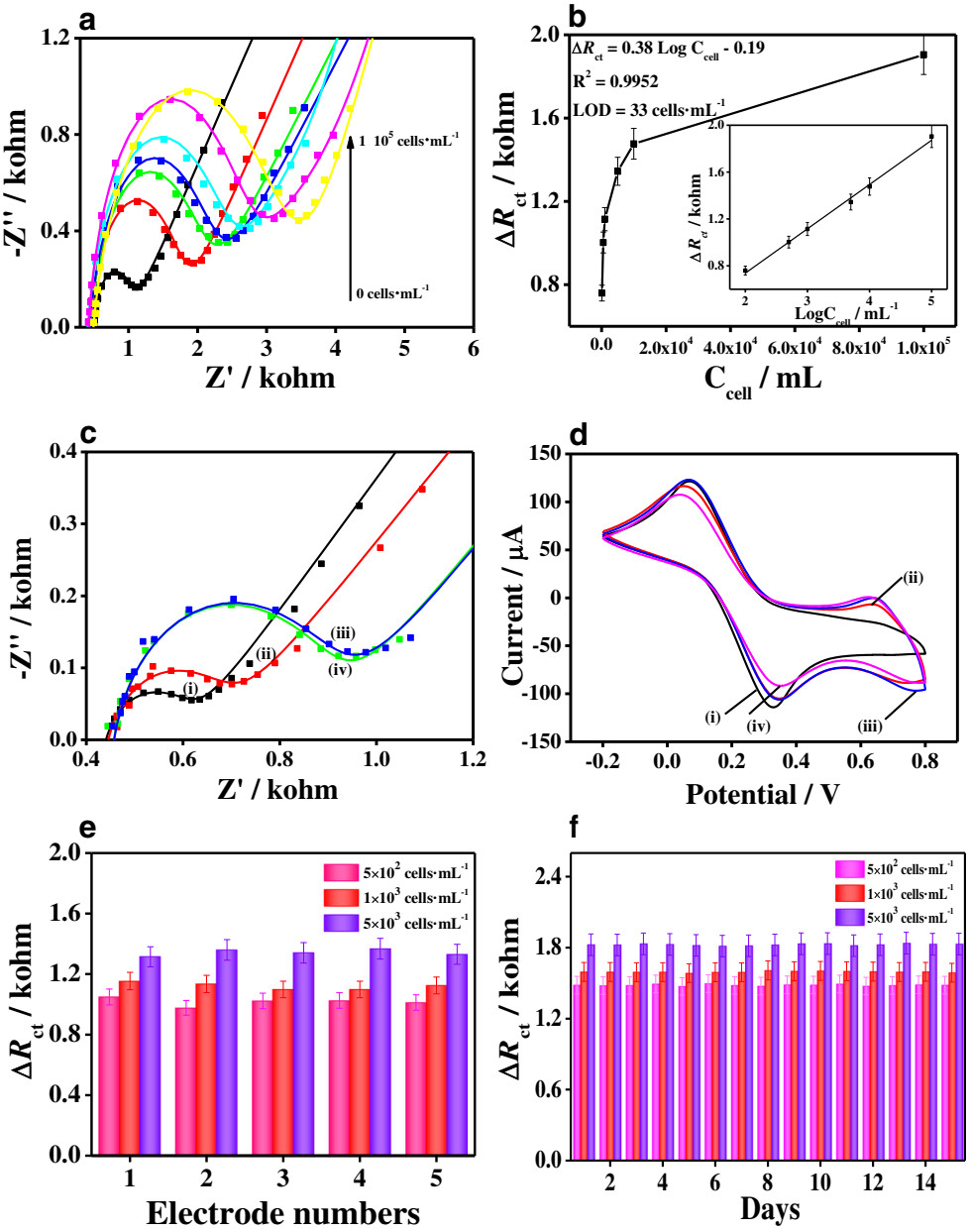

Fig. 5 (**a**) EIS responses of CoCu-ZIF@CDs-based cytosensor at different B16-F10 cell concentrations (0, 1×10^2, 5×10^2, 1×10^3, 5×10^3, 1×10^4 and 1×10^5 cells·mL^{-1}). (**b**) Dependence of ΔR_{ct} on the concentration of B16-F10 cells (inset: the linear parts of calibration plots, $n = 3$) (EIS measurement parameters: potential, 0.22 V; frequency range, 0.01 Hz–100 kHz; amplitude, 5 mV). (**c**) EIS Nyquist and (**d**) corresponding CV curves of the CoCu-ZIF@CDs nanohybrid modified AEs for detecting L929 cells in 0.01 M phosphate buffer (pH 7.4) containing 5.0 mM $[Fe(CN)_6]^{3-/4-}$, including (i) AE, (ii) CoCu-ZIF@CDs/AE, (ii) Apt/CoCu-ZIF@CDs/AE, and (iv) L929/Apt/CoCu-ZIF@CDs/AE. (**e**) The reproducibility of proposed cytosensor for B16-F10 cell detection at different concentrations (5×10^2, 1×10^3 and 5×10^3 cells·mL^{-1}). (**f**) The stability of the proposed cytosensor for B16-F10 cell detection (5×10^2, 1×10^3 and 5×10^3 cells·mL^{-1}) within 15 days

this cytosensor is that it only exhibits good selectivity toward normal cells and other cancer biomarkers.

The reproducibility of the CoCu-ZIF@CD-based electrochemical cytosensor was probed using five independently Apt/CoCu-ZIF@CDs/AE for detecting B16-F10 cells with different concentrations (5×10^2, 1×10^3, and 5×10^3 cells·mL^{-1}). As displayed Fig. 5e, the obtained ΔR_{ct} values show the relative stable values, giving the relative standard derivation (RSD) of current responses of 2.31% for detecting B16-F10 cells with the concentration of 5×10^2 cells·mL^{-1}, 1.89% for 1×10^3 cells·mL^{-1}, and 1.43% for 5×10^3 cells·mL^{-1}. This finding demonstrates good reproducibility of the cytosensor. Additionally, the stability of the cytosensor was investigated (Fig. 5f). The proposed cytosensor after detecting B16-F10 cancer cells with the concentrations of 5×10^2, 1×10^3, and 5×10^3 cells·mL^{-1} was stored in a refrigerator at 4 °C for 15 days and tested every day. It gives the low relative standard derivations (RSDs) of the cytosensor after detecting B16-F10 cells, 0.54% for 5×10^2 cells·mL^{-1}, 0.4% for 1×10^3 cells·mL^{-1}, and 0.4% for 5×10^3 cells·mL^{-1}. Thus, the stability of the cytosensor was satisfactory for detecting the cancer cells with different levels.

Conclusion

A novel electrochemical aptasensing strategy for detecting living B16-F10 cancer cells was constructed using 0D/2D

nanostructure of bimetallic CoCu-ZIF NSs and MXene-derived carbon quantum dots in this study. The efficient combination of CoCu-ZIF NSs and CDs endowed the CoCu-ZIF@CDs nanohybrid with some characteristic performances, such as better electrochemical activity, good fluorescence performance, stronger binding interaction toward aptamer strands, and higher stability of the formed complex of aptamer and B16-F10 cells. Compared with other MOF-based biosensors, the present CoCu-ZIF@CD-based one clearly illustrated three advantages: (i) the preparation feasibility of the 0D/2D CoCu-ZIF@CDs nanohybrid provides a new approach for developing novel electrode nanomaterial; (ii) good synergistic effect among different components of CoCu-ZIF@CDs nanohybrid makes the proposed cytosensor with some features of label-free, good biocompatibility, and excellent endocytosis; and (iii) electrochemical techniques and fluorescence imaging methods can determine the detection procedure of the proposed biosensor. Nevertheless, due to the weak specific recognition between aptamer strands and B16-F10 cancer cells, the CoCu-ZIF@CDs-based cytosensor shows poor selectivity in the presence of other cancer cells, but giving a high selectivity for normal cells or other biomarkers.

Supplementary Information The online version contains supplementary material available at https://doi.org/10.1007/s00604-021-04726-z.

Funding This work was supported by the Programs for the National Natural Science Foundation of China (NSFC: Account Nos. U1604127, 81601082, and 81371363) and China Postdoctoral Science Foundation (2019M660175).

Compliance with ethical standards

Conflict of interest The authors declare that they have no competing interests.

References

1. Nawaz M, Camussi G, Valadi H, Nazarenko I, Ekstrom K, Wang X, Principe S, Shah N, Ashraf NM, Fatima F, Neder L, Kislinger T (2014) The emerging role of extracellular vesicles as biomarkers for urogenital cancers. Nat Rev Urol 11(12):688–701
2. Liu HW, Chen L, Xu C, Li Z, Zhang H, Zhang X-B, Tan W (2018) Recent progresses in small-molecule enzymatic fluorescent probes for cancer imaging. Chem Soc Rev 47(18):7140–7180
3. Chang J, Wang X, Wang J, Li H, Li F (2019) Nucleic acid-functionalized metal-organic framework-based homogeneous electrochemical biosensor for simultaneous detection of multiple tumor biomarkers. Anal Chem 91(5):3604–3610
4. Swierczewska M, Liu G, Lee S, Chen X (2012) High-sensitivity nanosensors for biomarker detection. Chem Soc Rev 41(7):2641–2655
5. Huang P, Qian X, Chen Y, Yu L, Lin H, Wane L, Zhu Y, Shi J (2017) Metalloporphyrin-encapsulated biodegradable nanosystems for highly efficient magnetic resonance imaging-guided sonodynamic cancer therapy. J Am Chem Soc 139(3):1275–1284
6. Du L, Chen W, Wang J, Cai W, Kong S, Wu C (2019) Folic acid-functionalized zirconium metal-organic frameworks based electrochemical impedance biosensor for the cancer cell detection. Sensor Actuat B-Chem 301:127073
7. Wang M, Wang C, Liu Y, Hu B, He L, Ma Y, Zhang Z, Cui B, Du M (2020) Nonenzymatic amperometric sensor for hydrogen peroxide released from living cancer cells based on hierarchical $NiCo_2O_4$-$CoNiO_2$ hybrids embedded in partially reduced graphene oxide. Microchim Acta 187(8):436
8. Lv J, Zhao LJ, Qian RC, Long YT (2017) Off-on fluorescence monitoring of intracellular Ag^+ in single living cells using an Ag^+-responsive probe. Methods Appl Fluoresc 5:044003
9. Yan X, Song Y, Liu J, Zhou N, Zhang C, He L, Zhang Z, Liu Z (2019) Two-dimensional porphyrin-based covalent organic framework: a novel platform for sensitive epidermal growth factor receptor and living cancer cell detection. Biosens Bioelectron 126:734–742
10. He L, Li Z, Guo C, Hu B, Wang M, Zhang Z, Du M (2019) Bifunctional bioplatform based on NiCo Prussian blue analogue: label-free impedimetric aptasensor for the early detection of carcino-embryonic antigen and living cancer cells. Sensor Actuat B-Chem 298:126852
11. Zhou N, Su F, Li Z, Yan X, Zhang C, Hu B, He L, Wang M, Zhang Z (2019) Gold nanoparticles conjugated to bimetallic manganese(II) and iron(II) Prussian Blue analogues for aptamer-based impedimetric determination of the human epidermal growth factor receptor-2 and living MCF-7 cells. Microchim Acta 186(2):75
12. Cui L, Zhu BW, Qu S, He XP, Chen GR (2015) "Clicked" galactosyl anthraquinone on graphene electrodes for the label-free impedance detection of live cancer cells. Dyes Pigments 121:312–315
13. Gu C, Guo C, Li Z, Wang M, Zhou N, He L, Zhang Z, Du M (2019) Bimetallic ZrHf-based metal-organic framework embedded with carbon dots: ultra-sensitive platform for early diagnosis of HER2 and HER2-overexpressed living cancer cells. Biosens Bioelectron 134:8–15
14. Wang M, Hu M, Li Z, He L, Song Y, Jia Q, Zhang Z, Du M (2019) Construction of Tb-MOF-on-Fe-MOF conjugate as a novel platform for ultrasensitive detection of carbohydrate antigen 125 and living cancer cells. Biosens Bioelectron 142:111536
15. Kempahanumakkagari S, Deep A, Kim K-H, Kailasa SK, Yoon H-O (2017) Nanomaterial-based electrochemical sensors for arsenic-a review. Biosens Bioelectron 95:106–116
16. Zhang Y, Chen X (2019) Nanotechnology and nanomaterial-based no-wash electrochemical biosensors: from design to application. Nanoscale 11(41):19105–19118
17. Wu M-X, Yang Y-W (2017) Metal-organic framework (MOF)-based drug/cargo delivery and cancer therapy. Adv Mater 29:1606134
18. Liu L, Zhou Y, Liu S, Xu M (2018) The applications of metal-organic frameworks in electrochemical sensors. Chemelectrochem 5(1):6–19
19. Guselnikova O, Postnikov P, Elashnikov R, Miliutina E, Svorcik V, Lyutakov O (2019) Metal-organic framework (MOF-5) coated SERS active gold gratings: a platform for the selective detection of organic contaminants in soil. Anal Chim Acta 1068:70–79
20. Wang M, Hu M, Hu B, Guo C, Song Y, Jia Q, He L, Zhang Z, Fang S (2019) Bimetallic cerium and ferric oxides nanoparticles embedded within mesoporous carbon matrix: electrochemical immunosensor for sensitive detection of carbohydrate antigen 19-9. Biosens Bioelectron 135:22–29
21. Li XF, Yu SB, Yang B, Tian J, Wang H, Zhang DW, Liu Y, Li ZT (2018) A stable metal-covalent-supramolecular organic framework hybrid: enrichment of catalysts for visible light-induced hydrogen production. Sci China Chem 61(7):830–835

22. Li W, Lv S, Wang Y, Zhang L, Cui X (2019) Nanoporous gold induced vertically standing 2D NiCo bimetal-organic framework nanosheets for non-enzymatic glucose biosensing. Sensor Actuat B-Chem 281:652–658
23. Zhong G, Liu D, Zhang J (2018) The application of ZIF-67 and its derivatives: adsorption, separation, electrochemistry and catalysts. J Mater Chem A 6(5):1887–1899
24. Meng L, Xiao K, Zhang X, Du C, Chen J (2020) A novel signal-off photoelectrochemical biosensor for M.SssI MTase activity assay based on GQDs@ZIF-8 polyhedra as signal quencher. Biosens Bioelectron 150:111861
25. Pang J, Mendes RG, Bachmatiuk A, Zhao L, Ta HQ, Gemming T, Liu H, Liu Z, Rummeli MH (2019) Applications of 2D MXenes in energy conversion and storage systems. Chem Soc Rev 48(1):72–133
26. Zhou L, Wu F, Yu J, Deng Q, Zhang F, Wang G (2017) Titanium carbide ($Ti_3C_2T_x$) MXene: a novel precursor to amphiphilic carbide-derived graphene quantum dots for fluorescent ink, light-emitting composite and bioimaging. Carbon 118:50–57
27. Guan Q, Ma J, Yang W, Zhang R, Zhang X, Dong X, Fan Y, Cai L, Cao Y, Zhang Y, Li N, Xu Q (2019) Highly fluorescent Ti_3C_2 MXene quantum dots for macrophage labeling and Cu^{2+} ion sensing. Nanoscale 11(30):14123–14133
28. Cao Y, Wu T, Zhang K, Meng X, Dai W, Wang D, Dong H, Zhang X (2019) Engineered exosome-mediated near-infrared-II region V_2C quantum dot delivery for nucleus-target low-temperature photothermal therapy. ACS Nano 13(2):1499–1510
29. Sicco E, Baez J, Ibarra M, Moreno M, Cerecetto H, Calzada V (2020) Sgc8-c aptamer as a potential theranostic agent for hemato-oncological malignancies. Cancer Biother Radiopharm 35:262–270
30. Lai C, Gong M, Zhou Y, Fang J, Huang L, Deng Z, Liu X, Zhao T, Lin R, Wang K, Jiang K, Xin H, Wang D (2020) Sulphur modulated Ni_3FeN supported on N/S co-doped graphene boosts rechargeable/flexible Zn-air battery performance. Appl Catal B Environ 274:119086
31. Farka Z, Jurik T, Kovar D, Trnkova L, Skladal P (2017) Nanoparticle-based immunochemical biosensors and assays: recent advances and challenges. Chem Rev 117(15):9973–10042
32. Ding D, Yang C, Lv C, Li J, Tan W (2020) Improving tumor accumulation of aptamers by prolonged blood circulation. Anal Chem 92(5):4108–4114
33. Liu Y, Hu B, Wu S, Wang M, Zhang Z, Cui B, He L, Du M (2019) Hierarchical nanocomposite electrocatalyst of bimetallic zeolitic imidazolate framework and MoS_2 sheets for non-Pt methanol oxidation and water splitting. Appl Catal B-Environ 258:117970
34. Cui J, Liu J, Wang C, Rong F, He L, Song Y, Zhang Z, Fang S (2020) Efficient electrocatalytic water oxidation by using the hierarchical 1D/2D structural nanohybrid of CoCu-based zeolitic imidazolate framework nanosheets and graphdiyne nanowires. Electrochim Acta 334:135577
35. Yang X, Jia Q, Duan F, Hu B, Wang M, He L, Song Y, Zhang Z (2019) Multiwall carbon nanotubes loaded with MoS_2 quantum dots and MXene quantum dots: non-Pt bifunctional catalyst for the methanol oxidation and oxygen reduction reactions in alkaline solution. Appl Surf Sci 464:78–87
36. Xiao X, He C-T, Zhao S, Li J, Lin W, Yuan Z, Zhang Q, Wang S, Dai L, Yu D (2017) A general approach to cobalt-based homobimetallic phosphide ultrathin nanosheets for highly efficient oxygen evolution in alkaline media. Energy Environmen Sci 10(4):893–899
37. Fang Y, Liu Z, Han J, Jin Z, Han Y, Wang F, Niu Y, Wu Y, Xu Y (2019) High-performance electrocatalytic conversion of N_2 to NH_3 using oxygen-vacancy-rich TiO_2 in situ grown on $Ti_3C_2T_x$ MXene. Adv Energy Mater 9:1803406
38. Esmeryan KD, Castano CE, Bressler AH, Abolghasemibizaki M, Fergusson CP, Roberts A, Mohammadi R (2017) Kinetically driven graphite-like to diamond-like carbon transformation in low temperature laminar diffusion flames. Diam Relat Mater 75:58–68
39. Wang L, Chen L, Song P, Liang C, Lu Y, Qiu H, Zhang Y, Kong J, Gu J (2019) Fabrication on the annealed $Ti_3C_2T_x$ MXene/epoxy nanocomposites for electromagnetic interference shielding application. Compos Part B-Eng 171:111–118
40. Kakaei K, Hasanpour K (2014) Synthesis of graphene oxide nanosheets by electrochemical exfoliation of graphite in cetyltrimethylammonium bromide and its application for oxygen reduction. J Mater Chem A 2(37):15428–15436
41. Hu M, Cui C, Shi C, Wu Z-S, Yang J, Cheng R, Guang T, Wang H, Lu H, Wang X (2019) High-energy-density hydrogen-ion-rocking-chair hybrid supercapacitors based on $Ti_3C_2T_x$ MXene and carbon nanotubes mediated by redox active molecule. ACS Nano 13(6):6899–6905
42. Zhang X, Zhang H, Zhu H, Li C, Zhang N, Bao J, He G (2019) Co_3O_4 Nanorods with a great amount of oxygen vacancies for highly efficient Hg-0 oxidation from coal combustion flue gas. Energ Fuels 33(7):6552–6561
43. Yin J, Guo W, Qin X, Zhao J, Pei M, Ding F (2017) A sensitive electrochemical aptasensor for highly specific detection of streptomycin based on the porous carbon nanorods and multifunctional graphene nanocomposites for signal amplification. Sensor Actuat B-Chem 241:151–159
44. Cardoso AR, Cabral-Miranda G, Reyes-Sandoval A, Bachmann MF, Sales MGF (2017) Detecting circulating antibodies by controlled surface modification with specific target proteins: application to malaria. Biosens Bioelectron 91:833–841
45. Guo C, Li Z, Duan F, Zhang Z, Marchetti F, Du M (2020) Semiconducting Cu_xNi_{3-x}(hexahydroxytriphenylene)$_2$ framework for electrochemical aptasensing of C6 glioma cells and epidermal growth factor receptor. J Mater Chem B 8(43):9951–9960
46. Seven B, Bourourou M, Elouarzaki K, Constant JF, Gondran C, Holzinger M, Cosnier S, Timur S (2013) Impedimetric biosensor for cancer cell detection. Electrochem Commun 37:36–39
47. Kivrak E, Ince-Yardimci A, Ilhan R, Kirmizibayrak PB, Yilmaz S, Kara P (2020) Aptamer-based electrochemical biosensing strategy toward human non-small cell lung cancer using polyacrylonitrile/polypyrrole nanofibers. Anal Bioanal Chem 412(28):7851–7860
48. Liu D, Wang L, Ma S, Jiang Z, Yang B, Han X, Liu S (2015) A novel electrochemiluminescent immunosensor based on CdS-coated ZnO nanorod arrays for HepG2 cell detection. Nanoscale 7(8):3627–3633
49. Guo Y, Shu Y, Li A, Li B, Pi J, Cai J, Cai H-H, Gao Q (2017) Efficient electrochemical detection of cancer cells on in situ surface-functionalized MoS_2 nanosheets. J Mater Chem B 5(28):5532–5538
50. Chowdhury AD, Ganganboina AB, Tsai YC, Chiu HC, Doong RA (2018) Multifunctional GQDs-Concanavalin A@Fe_3O_4 nanocomposites for cancer cells detection and targeted drug delivery. Anal Chim Acta 1027:109–120
51. Li L, Han B, Wang Y, Zhao J, Cao Y (2019) Simple and universal signal labeling of cell surface for amplified detection of cancer cells via mild reduction. Biosens Bioelectron 145:111714
52. Yang Y, Fu Y, Su H, Mao L, Chen M (2018) Sensitive detection of MCF-7 human breast cancer cells by using a novel DNA-labeled sandwich electrochemical biosensor. Biosens Bioelectron 122:175–182